Influence of cohesive clay on wave–current ripple dynamics captured in a 3D phase diagram

XuxuWu[1,2], Jonathan Malarkey[3], Roberto Fernández[4], Jaco Baas[3], Ellen Pollard[1], and Daniel Parsons[5]

[1]Energy and Environment Institute, University of Hull, Hull, HU6 7RX, UK.
5   [2]School of Environmental Sciences, University of Hull, Hull, HU6 7RX, UK.
[3]School of Ocean Sciences, Bangor University, Menai Bridge, LL59 5AB, Wales, U.K.
[4]Department of Civil and Environmental Engineering, The Pennsylvania State University, State College, PA 16802, USA.
[5]Loughborough University, Loughborough, LE11 3TU, U.K.

10   *Correspondence to*: Xuxu Wu (x.wu@hull.ac.uk)

Abstract. Wave–current ripples that develop on seabeds of mixed non-cohesive sand and cohesive clay are commonplace in coastal and estuarine environments. However, laboratory research on ripples forming in these types of mixed-bed environments is relatively limited. New large-scale flume experiments seek to address this by considering two wave-current conditions with initial clay content, 15 C_0, ranging from 0 to 18.3%. The experiments record ripple development and pre- and post-experiment bed clay contents, to quantify clay winnowing. The experiments are combined with previous data to produce a consistent picture of larger and smaller flatter ripples over a range of wave-current conditions and C_0. Specifically, the results reveal a sudden decrease in the ripple steepness for $C_0 > 10.6\%$, likely associated with hydraulic conductivity. Accompanying the sudden change in steepness is a gradual 20   linear decrease in wavelength with C_0 for $C_0 > 7.4\%$, which may be significant for paleoenvironmental reconstruction. Moreover, for a given flow, the initiation time, when ripples first appear on a flat bed, increases with increasing C_0. This, together with the fact that the bed remains flat for the highest values of C_0, demonstrates that the threshold of motion increases with C_0. The inferred threshold enhancement, and the occurrence of large and small ripples, is used to construct a new three-dimensional phase 25   diagram of bed characteristics involving the wave and current Shields parameters and C_0, which has important implications for morphodynamic modelling. Winnowing occurs for both flat and rippled beds, but the rate is two orders of magnitude smaller for flat beds.

1 Introduction

Combined wave–current flows form ripples on the seabed that are ubiquitous in coastal and estuarine
environments, including continental shelves, the shoreface, and tidal flats (e.g., Osborne and
Greenwood, 1993; Li and Amos, 1999; Héquette et al., 2008; Gao, 2019). Ripple dynamics play a
crucial role in sediment transport, which in turn affects the predictions of large-scale coastal
morphodynamic numerical models (Brakenhoff et al., 2020), the underwater scour around civil
engineering structures (Sumer et al., 2001), and the transport of nutrients and contaminants (Vercruysse
et al., 2017). It is therefore important to fully understand how combined-flow hydrodynamics control
ripple dimensions and vice versa ~~for coastal and estuarine management and ecological balance
maintenance,~~ especially as such areas may face more extreme weather events in the context of climate
change and sea level rise (e.g., Mousavi et al., 2011, Vitousek et al., 2017). Moreover, combined-flow
ripples have been found in the geological record, thus providing key information for reconstructing
paleoenvironments (e.g., Myrow et al., 2006, Beard et al., 2017).

Sediment transport prediction and environmental reconstruction are dependent on ripple predictors that
include bedform phase diagrams and empirical formulae. Phase diagrams group similar bedform types
and cross-sectional geometries for known hydrodynamic conditions and sediment properties (e.g., Van
den Berg and Van Gelder, 1993). In the last thirty years, a substantial number of experimental studies
has made progress in compiling combined-flow ripple phase diagrams (Arnott and Southard, 1990,
Kleinhans, 2005, Dumas et al., 2005, Cummings et al., 2009, Perillo et al., 2014). Using a range of
combined-flow conditions in an experimental flume, Perillo et al. (2014) expanded the bedform phase
diagrams of Arnott and Southard (1990) and Dumas et al. (2005) by subdividing bedform types based
on planform geometry. Baas et al.'s (2021) phase diagram, based on field observations of bedforms on
an intertidal flat in the Dee Estuary, U.K., captured bedform types generated under a wider range of
flow conditions, including those generated under waves and currents at angles to one another.
Compared to wave-alone and current-alone ripple predictors, relatively few predictors are available for
combined flow ripples. Tanaka and Dang (1996) modified a widely used predictor for wave ripples
developed by Wiberg and Harris (1994) by considering the influence of grain size and the relative
strength of the wave and current velocities on the ripple size. Khelifa and Ouellet (2000) developed a

new formulation to predict ripple dimensions by introducing an effective combined-flow mobility parameter.

To date, however, it is unclear if these ripple predictors developed for well-sorted sand work for combined-flow ripples in muddy coastal and estuarine environments that are widespread in nature

60 (Healy et al., 2002). Wu et al. (2022) were the first to consider ripple dynamics in sand–clay mixtures under combined flows and revealed the formation of small flat ripples with an initial clay content, C_0, greater than 10.6% under hydrodynamic conditions that would generate large equilibrium ripples in clean sand. Moreover, Wu et al. (2022) demonstrated that clay winnowing efficiency played a significant role in the development towards clean-sand-like ripples from mixed sand–clay beds (Baas et

65 al., 2013, Wu et al., 2018) and highlighted the process of deep cleaning of clay below ripple troughs. Wu et al. (2022) also found that the clay loss rate from the bed was much lower when $C_0 > 10.6\%$, as the stronger cohesion resisted further ripple development. The experiments of Wu et al. (2022) were conducted under a single wave-dominated combined-flow condition, but further study considering wider hydrodynamic conditions are required for the development of morphodynamic models in muddy

70 estuaries and the coastal zone.

Therefore, the present study extends Wu et al.'s (2022) experiments and describes a systematically collected set of data from large-scale flume experiments on ripple development. This study also draws in available sand–clay experiments under current-alone and wave-alone conditions (Baas et al., 2013; Wu et al, 2018). The three specific objectives of this study were: (1) to compare ripple development on

75 beds with similar clay content under different hydrodynamic conditions; (2) to compare clay winnowing efficiency, based on quantifying bed clay content during ripple development, under different flow conditions; and (3) to propose a new phase diagram for bedforms generated in sand–clay substrates.

2 Materials and Methods

2.1 Experiment setup

80 The experiments were undertaken in a recirculating flume tank in the Total Environment Simulator at the University of Hull. Three equal-size channels, 11 m long and 1.6 m wide, were separated by brick

walls, 0.2 m high, in the tank (Figure 1). Combined flow conditions were maintained during the experiments and flow velocities in each channel were measured by a 25 Hz Vectrino profiler. Freshwater was used in all experiments, and the water depth, h, was set to 0.4 m. A 2-MHz ultrasonic

85   ranging sensor (URS), containing 32 probes, monitored the ripple evolution and migration in the test section (Figure 1). Further details of the instrument setup are available from Wu et al. (2022).
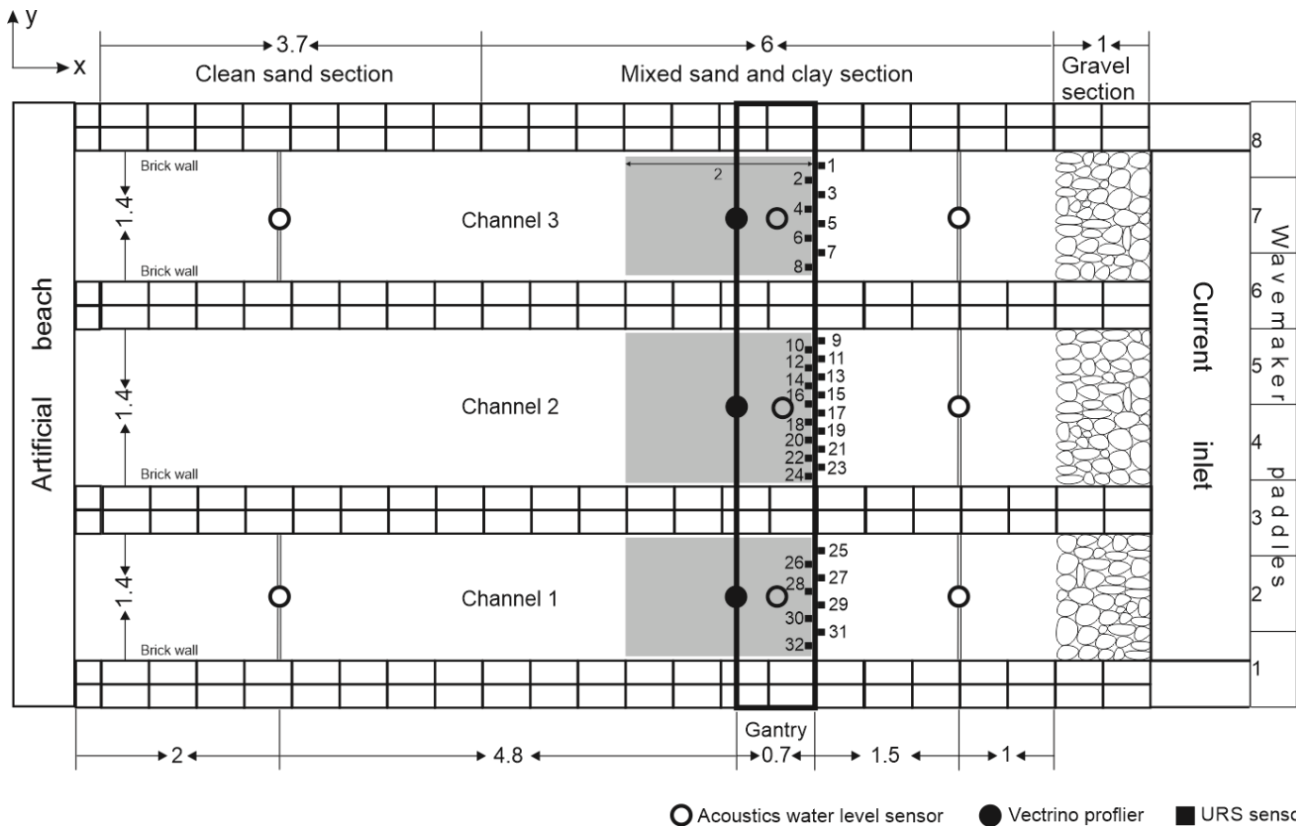
Figure 1.   Plan view of the experimental setup. The grey area was scanned by an Ultrasonic Range System (URS) with numbered sensors (black squares). White and black circles denote acoustic

90   water level sensors and Vectrino profilers, respectively. Dimensions are in metres.

2.2 Experimental procedure and wave–current settings

To complement Wu et al.'s (2022) wave-dominated flow condition, with depth-average current, $U_c \approx$ 0.16 m s^{-1}, and wave velocity amplitude, $U_o \approx 0.32$ m s^{-1}, (Table A1), the present experiments comprised two additional flow conditions of increased relative current strength, with $U_c \approx 0.3$ m s^{-1} and

95 $U_o \approx 0.27$ and 0.13 m s^{-1}, with wave heights, H, of 0.05 and 0.1 m, and wave period, T, of 2 s (Table 1).
The flow conditions are numbered according to increasing relative current strength from WC1 (Wu et
al., 2022) to WC2 and WC3 (Table 1). The experiments involved different initial mass concentrations
of clay, C_0, in each of the three channels, with the same flow conditions for each channel. The bed was
composed of a well-sorted sand with a median diameter, D_{50}, of 0.45 mm and cohesive kaolinite clay

100 with $D_{50} = 0.0089$ mm. The sand, clay, water depth and wave period in the present experiments were
the same as in Wu et al. (2022). The order of the experiments was from high to low clay content, by
taking advantage of the natural winnowing of the bed during the experiments. Run 1, the sand-only
control, and Run 2, with C_0 of 9.9%, 13.1%, and 18.3% in channels 1 to 3, were under WC3 flow
conditions (Table 1). The beds in Run 2 remained essentially flat after 650 min. In Run 3, the wave

105 height was doubled (WC2) and the duration was increased to 1850 min. In Run 4, three beds were
prepared with relatively low clay contents, $C_0 \leq 6.4\%$, and the same WC3 conditions as in Runs 1 and 2
were imposed.

To ensure homogeneity in the mixed section of each channel (Figure 1), the clay was mixed into the
sand using a handheld plasterer's mixer and the sediment beds were flattened using a wooden leveller

110 between runs. A terrestrial 3D laser scanner (FARO Focus3D X330) was used to scan the sediment bed
in each channel before and after the run, after the water had been drained. Furthermore, the flow was
temporarily stopped during the runs at pre-set times to make URS bed scans and collect sediment cores
from the bed using syringes with a diameter of 20 mm and a maximum length of 90 mm. Details of the
protocols for URS bed scanning and sediment core collection are available from Wu et al. (2022).

115 Channel 2 of Run 4 was excluded from the analysis, because the sediment in this channel was not
sufficiently well mixed.

Wu et al. (2022) justified their choice of flow conditions by demonstrating that they were largely
consistent with the observations of Baas et al.'s (2021) intertidal field site in the macrotidal Dee Estuary
(U.K.), where $D_{50} = 0.227$ mm, $0 < h \leq 3.5$ m, $0 < U_c \leq 0.6$ m/s, $0 < U_o \leq 0.45$ m/s and $0 < C_0 \leq 14\%$.

120 Baas et al. (2021) produced a phase diagram based on the equivalent wave-only and current-only skin
friction, τ_w and τ_c, using Malarkey and Davies' (2012) shear stress calculation with the strong non-linear
option. Here in Figure 2, Baas et al.'s (2021) phase diagram has been non-dimensionalised to the

equivalent wave-only and current-only Shields parameters, θ_w and θ_c, given by $\tau/(\rho_s-\rho)gD_{50}$, where ρ_s is the sediment density (= 2650 kg m^{-3}), ρ is the water density (= 1000 kg m^{-3} for freshwater, 1027 kg m^{-3}

125 for seawater) and g is the acceleration due to gravity (= 9.81 m s^{-2}). This allows the present experiments (Table 1, WC2 and WC3) and previous wave–current experiments (WC1, Table A1), together with the current-alone and wave-alone experiments of Baas et al. (2013) and Wu et al. (2018) (Tables A2 and A3), to be compared to one another. In Figure 2, the critical Shields parameter for the clean-sand threshold of motion, θ_0, is determined with Soulsby's (1997) formula, $\theta_0 = 0.3/(1+1.2D_*) + 0.055[1-$

130 $\exp(-0.02D_*)]$, where $D_* = D_{50}[(\rho_s-\rho)gv^2/\rho]^{1/3}$ and v is the kinematic viscosity of water. It should be noted that the threshold of motion is different for each grain size: $\theta_0 = 0.032$ for WC1-WC3, $D_{50} = 0.45$ mm, and Wu et al. (2018), $D_{50} = 0.496$ mm; $\theta_0 = 0.061$ for Baas et al. (2013), $D_{50} = 0.143$ mm; and $\theta_0 = 0.05$ for Baas et al. (2021), $D_{50} = 0.227$ mm. In Figure 2 the threshold of motion appears as a straight line given by $\theta_w+\theta_c = \theta_0$ because, unlike in the field study of Baas et al. (2021), all experimental flows

135 were co-linear. Whilst θ_0 is clearly affected by grain size, it is assumed that the other boundaries in the phase diagram are not.

The phase diagram (Figure 2) identifies the flow conditions of Wu et al. (2018) and WC1 as wave-dominated (W), $\theta_c < 0.2\theta_w$, those of Baas et al. (2013) as current-dominated (C), $\theta_c > 3.3\theta_w$ and those of the present experiments (WC2 and WC3) as wave-current (WC), $0.2\theta_w < \theta_c < 3.3\theta_w$. Whilst not all

140 experiments produced ripples (open circles and NR in Table 1), all the data were between the washout limit $\theta_w+\theta_c = 0.18$ and the clean-sand threshold of motion, $\theta_w+\theta_c = \theta_0$. The reason that not all conditions produce ripples is related to higher clay contents enhancing the threshold shear stress. This is a shortcoming of the phase diagram of Baas et al. (2021) and is the justification for the new phase diagram proposed in this paper.

145 Table 1 Experimental parameters

Run/ Channel	Flow code[1]	Duration (min)	C_0 (%)	H (m)	U_o (m s^{-1})	U_c (m s^{-1})	θ_w	θ_c	Bed description[2]
1/2	WC3	600	0	0.05	0.14	0.31	0.047	0.031	R
2/1	WC3	650	9.9	0.05	0.13	0.31	0.042	0.031	NR
2/2	WC3	650	13.1	0.05	0.14	0.29	0.047	0.027	NR

2/3	WC3	650	18.3	0.05	0.13	0.31	0.042	0.031	NR
3/1	WC2	1850	8.4	0.1	0.27	0.32	0.124	0.033	R
3/2	WC2	1850	10.8	0.1	0.27	0.30	0.124	0.029	R
3/3	WC2	1850	16.3	0.1	0.27	0.31	0.124	0.031	NR
4/1	WC3	1250	2.5	0.05	0.13	0.25	0.042	0.020	R
4/3	WC3	1250	6.4	0.05	0.12	0.29	0.037	0.027	R

[1]Larger number in flow code represents stronger current compared to WC1 (the wave-dominated flow of Wu et al., 2022).

[2]R - ripples formed and NR - no ripple formed.

2.3 Data processing

150 Raw bed elevation profiles recorded from each URS scan, consisting of 16 profiles for channel 2 and 8 profiles for channels 1 and 3, were processed after de-spiking and smoothing. A Matlab 'peaks and troughs' tool was used to identify individual ripple heights, η, and wavelengths, λ, followed by calculation of the mean values of λ_t and η_t at a bed scanning time of t to construct the development curves of ripple height and wavelength and hence determine equilibrium bedform dimensions.

155 Following Wu et al. (2022), the equilibrium ripple height, η_e, and wavelength, λ_e, and equilibrium time for ripple height, T_η, and wavelength, T_λ, were calculated using the procedure of Baas et al. (2013), which includes a delay time for the first appearance of ripples, t_i, and an initial wavelength, λ_i:

$$\frac{\eta_t}{\eta_e} = 1 - 0.1^{\frac{t-t_i}{T_\eta - t_i}}, \qquad (1)$$

$$\frac{\lambda_t - \lambda_i}{\lambda_e - \lambda_i} = 1 - 0.1^{\frac{t-t_i}{T_\lambda - t_i}}. \qquad (2)$$

The ripples were also characterised by their steepness, RS, and ripple symmetry index, RSI, given by

$$RS = \eta_e / \lambda_e, \qquad (3)$$

$$RSI = \lambda_s / \lambda_l, \qquad (4)$$

where λ_s and λ_l are the length of the stoss and lee side of the ripple (RSI < 1.3 for symmetric and 1.3 <

160 RSI < 1.5 for quasi-asymmetric ripples, Perillio et al., 2014) (Table 2).

Sediment cores from the initial flat bed and the ripple crests and troughs were sliced into 10-mm intervals for grain-size analysis using a Malvern Mastersizer 2000. In the crest cores. the region corresponding to the active layer (ripple crest down to trough) were sliced into 5-mm intervals for better resolution of the clay content within the ripples. The measured clay content, C, in the sediment cores was further processed to acquire the total amount of clay removed from the bed, I, by integrating the clay deficit, defined as $C_{def} = C_0 - C$, from the lowest reference level, $z = -100$ mm up to the crest level, $z = 0$ mm. These quantities allow the equivalent clean-sand depth, d_c, to be given by

$$d_c = I/C_0, \tag{5}$$

which is the amount of clean sand available in the uppermost layers for ripple growth. Finally, the sediment concentration profiles were characterised by a Gaussian-type function. Full details of all data processing are available from Wu et al. (2022).
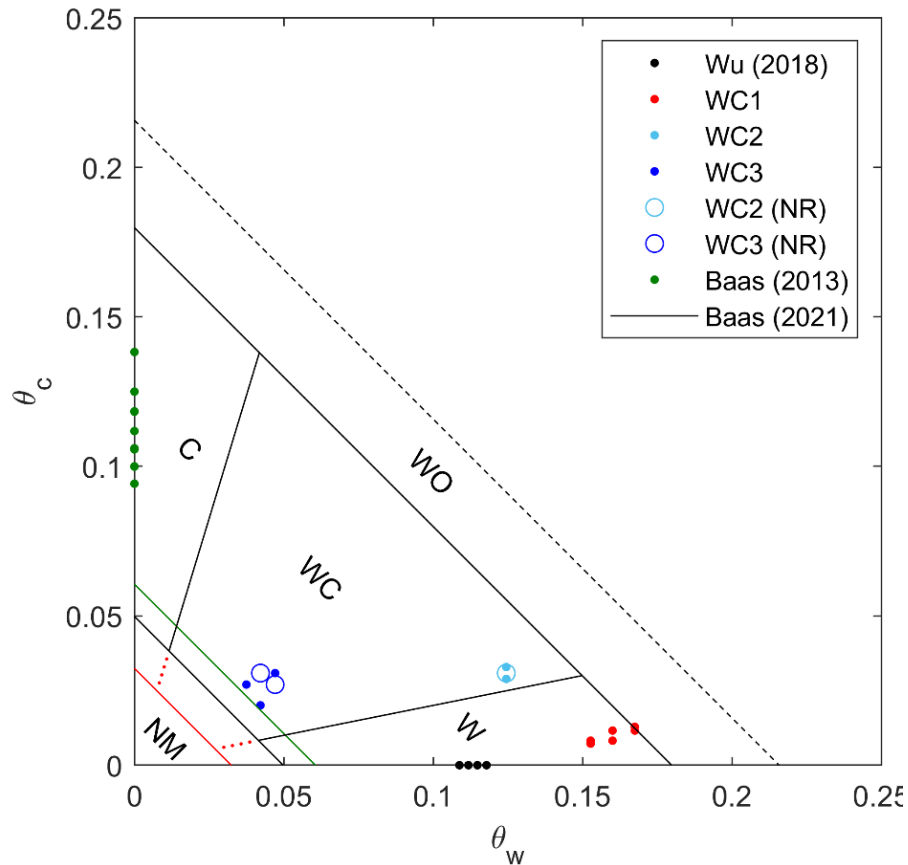
Figure 2.   Non-dimensional, θ_w-θ_c phase diagram after Baas et al. (2021), showing all wave-only

(Wu et al., 2018), wave-current (WC1-WC3), and current-only (Baas et al., 2013) conditions.

Open circles show cases where no ripples (NR) were present, and the various regions are

175   marked C - current-dominant, WC - wave-current, W - wave-dominant, NM - no motion and

WO - washout. The threshold of motion lines, θ_0, are coloured red for WC1-WC3 and Wu et al.

(2018) and green for Baas et al. (2013).

3. Results

3.1 Ripple development

180   Figure 3 shows the development of ripple height and wavelength for different C_0-values in the present

experiments (WC2 and WC3). For $C_0 = 0\%$ (WC3), clean-sand ripples were generated immediately

after the start of the experiment, hence $t_i = 0$, followed by rapid growth of the ripples. Equilibrium

ripple height, $\eta_e = 15.5$ mm, was reached at $T_\eta = 53$ min, whilst the equilibrium ripple wavelength, $\lambda_e =$

147.9 mm, required a longer $T_\lambda = 302$ min (Figure 3a and b; Table 2). As shown in Figure 4a, the clean-

185   sand ripples were two-dimensional in plan view, with straight continuous crestlines. In cross-section,

these ripples were quasi-asymmetric, with a ripple symmetry index (RSI) of 1.4 and a ripple steepness

(RS) of 0.11 (Table 2).
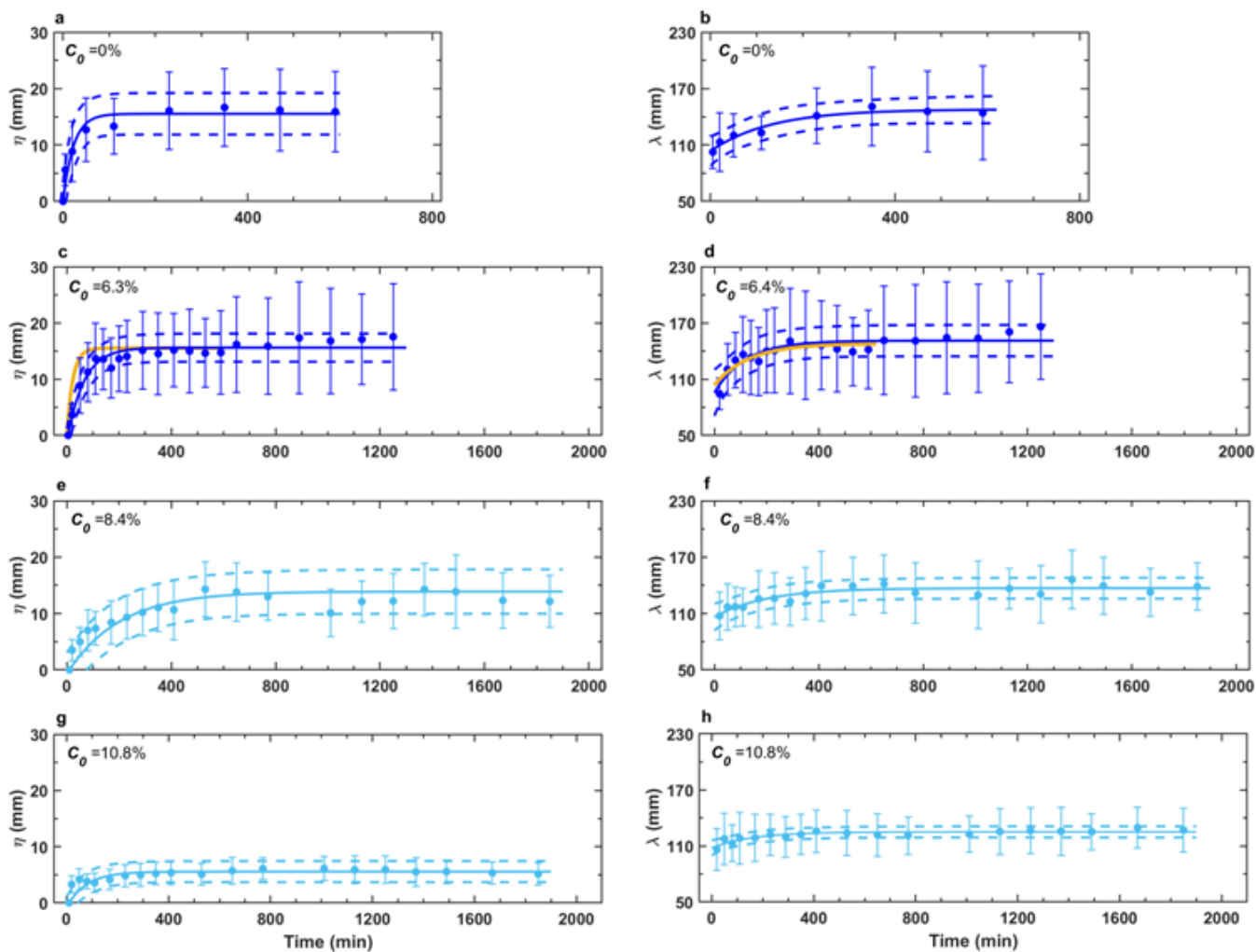
Figure 3. Development of ripple height and wavelength for WC3 (dark blue dots in a – d) and
190   WC2 (light blue dots in e - f) for different values of C_0. The error bars denote one standard
deviation from the mean dimension. Continuous dark and light blue lines are based on fitting to
Equations 1 and 2, and dashed dark and light blue lines are their corresponding 95% confidence
intervals. The yellow lines are the best-fit curves for clean sand (a, b).
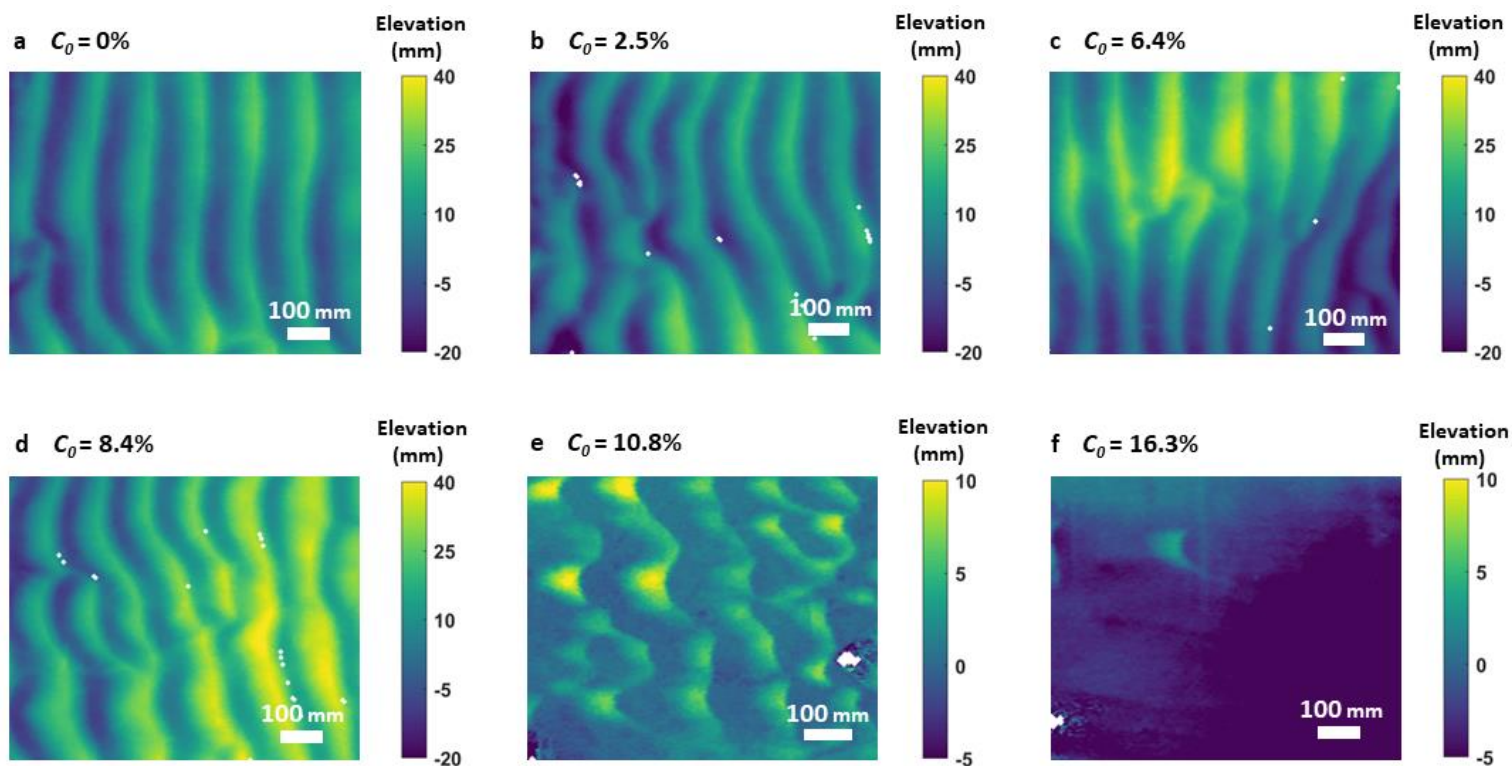
195 Figure 4. Plan view of ripple morphology in the test section acquired by the 3D FARO scanner at the end of the experiment. a – c: rippled beds formed under WC3 conditions; d – f: bed states under WC2 conditions. C_0 is the initial clay content and the flow direction is from left to right. Note elevation scales in E and F are different from those in a – d.

For C_0 = 2.5 and 6.4% (WC3), the ripples developed to similar equilibrium dimensions as their clean-sand counterparts, η_e = 15.6 mm and λ_e = 152.5 mm for C_0 = 6.4% (Figure 3c and d), and the bed was again covered in two-dimensional, quasi-asymmetric ripples (Figure 4b and c). However, the ripples developed more slowly compared to their clean-sand counterparts, especially for the ripple height, with T_η approximately tripled to 151 min (Table 2, C_0 = 6.4%).

The three WC3 cases with $C_0 \geq 9.9\%$ remained flat over the entire ten-hour duration (Table 2), implying there was no sand movement in these cases. Despite flat-bed conditions persisting, winnowing during the experiment caused the bed clay content to decrease, as will be seen in the next section, such that the initial clay contents were C_0 = 8.4, 10.8 and 16.3% for the three channels in the subsequent run under WC2 conditions, where U_o was doubled to 0.27 m s^{-1}. For C_0 = 8.4% (WC2), small ripples appeared at t = 10 min and by t = 20 min they had reached a height and wavelength of 3.5 mm and 107.3 mm, respectively. Thereafter, ripple dimensions developed gradually over a period of around seven hours, before stabilising (Figure 3e and f). Equations 1 and 2 predict ripple equilibrium height and wavelength of 13.9 and 137 mm, and equilibrium time for the ripple height and wavelength were 471 and 465 min. The equilibrium ripples retained similar geometries to those developed under WC2 conditions, characterised by two-dimensional plan forms with quasi-asymmetric cross sections (Table 2; Figure 4d). At C_0 = 10.8% (WC2), small ripples again appeared at t = 10 min and by t = 20 min they had reached a height of 3.3 mm. This was followed by a period of slow growth up to a height of 5 mm at t = 200 min; thereafter, the ripple height exhibited limited growth, only attaining a maximum of η_e = 5.6 mm at T_η = 273 min (Figure 3g, Table 2). The corresponding equilibrium wavelength was λ_e = 125 mm at T_λ = 377 min (Figure 3h, Table 2). The small ripples formed at C_0 = 10.8% (WC2) were three-dimensional with discontinuous, sinuous crestlines in plan view. In cross-section, these ripples were asymmetric and flatter, with RSI = 1.6 and RS = 0.04 (Figure 4e, Table 2). For the C_0 = 16.3% (WC2) case, the bed remained flat (Figure 4f); there was no sand movement.

223   Table 2. Bedform characteristics

Flow ID	C_0 (%)	Bedform type	η_e (mm)	T_η (min)	R^2	λ_e (mm)	λ_i (mm)	T_λ (min)	R^2	t_i (min)	RSI	RS
WC3	0	QAR	15.5 ± 1.5	53	0.95	147.9 ± 9.4	103.5 ± 10.2	302	0.95	0	1.5 ± 0.4	0.11 ± 0.03
WC3	2.5	QAR	14.8 ± 0.68	71	0.91	144.8 ± 5.5	99.1 ± 11.7	330	0.8	0	1.5 ± 0.5	0.11 ± 0.04
WC3	6.4	QAR	15.6 ± 0.67	151	0.94	152 ± 5.9	105 ± 14.8	344	0.79	5	1.5 ± 0.4	0.1 ± 0.04
WC3	9.9	NR	–	–	–	–	–	–	–	–	–	–
WC3	13.1	NR	–	–	–	–	–	–	–	–	–	–
WC3	18.3	NR	–	–	–	–	–	–	–	–	–	–
WC2	8.4	QAR	13.9 ± 1.29	471	0.80	137 ± 3.7	107.7 ± 8.6	465	0.79	10	1.4 ± 0.4	0.09 ± 0.03
WC2	10.8	AR	5.6 ± 0.2	273	0.96	125 ± 1.9	108.9 ± 5	377	0.79	10	1.6 ± 0.5	0.04 ± 0.01
WC2	16.3	NR	–	–	–	–	–	–	–	–	–	–

224   QAR: Quasi-Asymmetric Ripple

225   AR: Asymmetric Ripple

226   NR: No Ripples

227   R^2: Squared correlation coefficient of the best fit curve

228   ±: Standard deviation

3.2 Comparison of pre- and post-experiment vertical bed clay content

230 Figure 5 shows the pre- and post-experiment, vertical clay content in the bed, based on grain-size analysis of the sediment cores. In each case, the vertical grey solid and dashed lines show the value of $C_0 \pm$ one standard deviation. Figure 5a–d show the pre-experiment clay contents and Figure 5e–h show the post-experiment clay contents for WC3. The three WC3 flat-bed cases (Figure 5f–h) were used as the pre-experiment cores for WC2, with post-experiment cores shown in Figure 5i–k. For WC3, $C_0 =$

235 6.4%, the sediment cores show a 100% clay loss in the active layer (ripple crest down to the ripple trough level) and an additional layer of substantial clay loss with a thickness of c. 80 mm below the active layer (Figure 5e). The equivalent clean-sand depth (black horizontal dashed line), $d_c = I/C_0$, was 57 mm, more than two times the ripple height (25 mm). For WC2, $C_0 = 8.4\%$ (Figure 5i), a small amount of clay, 2.9%, remained at the base of the active layer. In contrast to the $C_0 = 6.4\%$ case, $d_c =$

240 13.1 mm is smaller than the ripple height (17.5 mm). For $C_0 = 10.8\%$ (Figure 5j), there were much smaller ripples (Figure 3g and h, and Table 2), which contained a higher clay content of 8% at the base of the active layer. Here, $d_c = 10.1$ mm, compared to the ripple height of 5.6 mm.

No ripples formed for $C_0 \geq 9.9\%$ under WC3 conditions and $C_0 = 16.3\%$ under WC2 conditions (Table 2). Nevertheless, the post-experiment sediment cores clearly demonstrate clay loss at all measured

245 depths (Figure 5 f–h, and k). Specifically, there was an approximate 10% reduction in clay content on beds with $C_0 = 16.3\%$ and 18.3%, whereas there was a higher percentage of clay loss from the lower C_0 beds: 15% for $C_0 = 9.9\%$ and 18% for $C_0 = 13.1\%$. This difference is reflected in the d_c values: 15 and 19 mm for $C_0 = 9.9\%$ and 13.1% compared to 14 and 11 mm for $C_0 = 16.3\%$ and 18.3%.
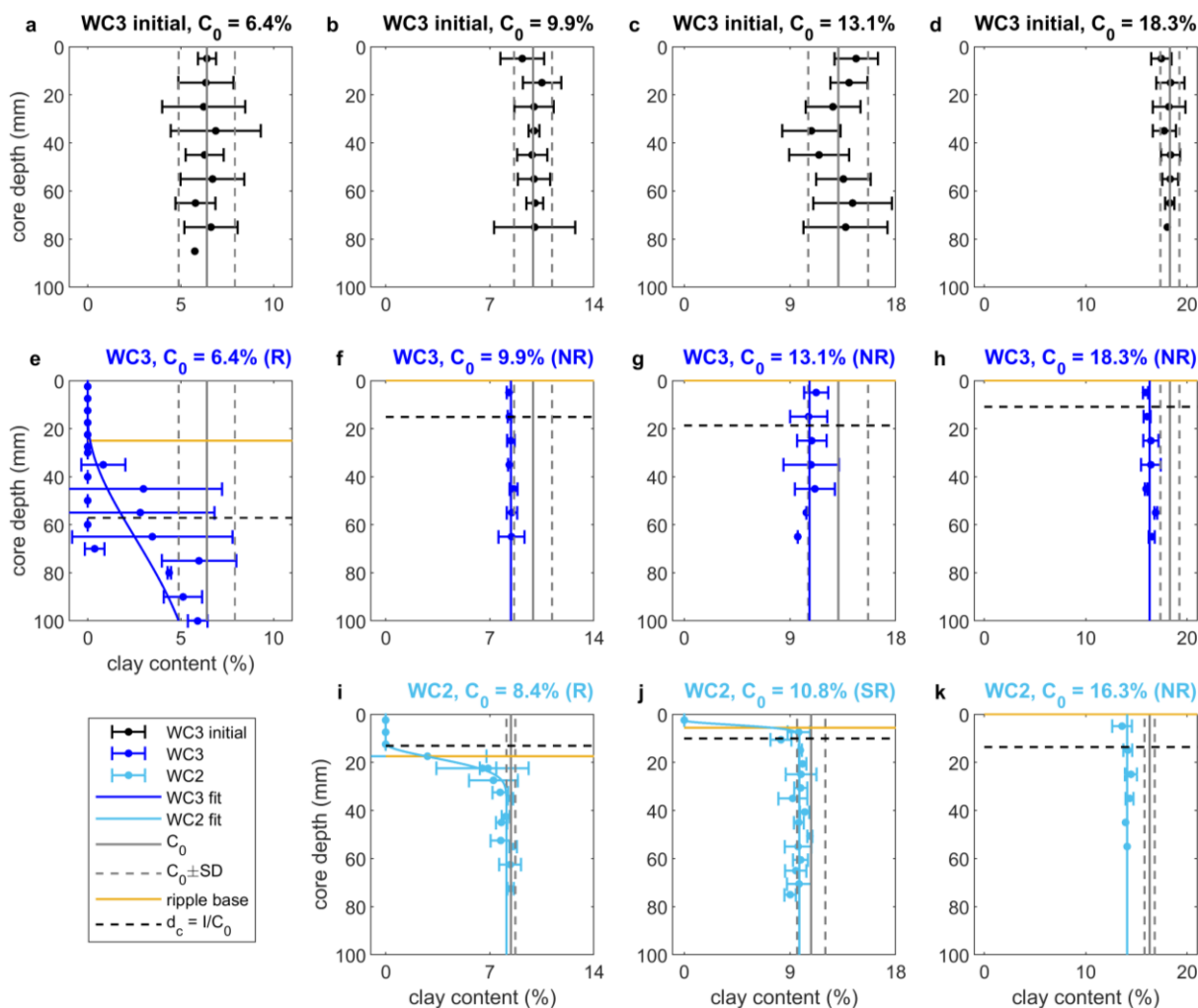
Figure 5. Pre-and post-experiment vertical profiles of clay content in cores collected from beds in the mixed sand–clay section. In each case, the pre- and post-experiment profiles are directly above one another: for WC3 conditions (pre- a–d and post- e–h) and for WC2 conditions (pre- f–h and post- i–k). Note the three WC3 flat-bed cases (f–h) were used as the pre-experiment cores for WC2 (i–k). The dark/light blue solid lines are the fits to WC3/WC2 post-experiment clay contents at each depth. The grey vertical solid and dashed lines represent mean initial clay content, C_0, and one standard deviation from the mean for comparison. The horizontal error bars denote one standard deviation of the mean clay content at that depth. For post-experiment cores, the yellow lines represent the ripple base and the dashed horizontal black lines represent the equivalent clean-sand depth.

4 Discussion

4.1 The effect of clay and hydrodynamic conditions on ripple dimensions and geometries

Wu et al.'s (2022) experiments, under WC1 flow conditions, revealed two distinct types of equilibrium ripples with a threshold C_0 value of 10.6%. For $C_0 \leq 10.6\%$, large 2D ripples with similar dimensions and geometries to their clean-sand counterparts developed, whereas for $C_0 > 10.6\%$ only small flat 3D ripples developed. In the present experiments under WC2 conditions, this discontinuity in equilibrium ripple size was also observed (Table 2), with small equilibrium ripples generated in the $C_0 = 10.8\%$ case, consistent with $C_0 > 10.6\%$. Additionally, the clay content at the base of the active layer was c. 8%, which is consistent with Wu et al.'s (2022) threshold that restricts the ripples from growing beyond their small, flat stage. Wu et al. (2022) argued that this latter 8% threshold was more general than the $C_0 = 10.6\%$ threshold as it was found to be also the case at the base of the active layer for Baas et al.'s (2013) $C_0 = 13\%$ threshold for fine-sand current ripple sizes (Table A2).

Figure 6a, which includes WC1-WC3 and Wu et al.'s (2018) wave-only cases, shows that the two ripple types correspond to two quite distinct constant steepness groupings, RS, which change at $C_0 = 10.6\%$. For WC3 conditions, the $C_0 = 10.6\%$ small–large ripple threshold is hypothetical as the bed shear stresses for what would be small ripples are below the threshold of motion for $C_0 \geq 9.9\%$, hence no ripples form (RS = 0). The threshold of motion will be discussed in the next section. Figure 6a demonstrates another feature of the larger wave-only and wave–current ripples which can also be seen in the data of Perillo et al. (2014). The steepness is directly related to the current shear stress: RS = 0.145 for Wu et al. (2018), where $\theta_c = 0$; RS = 0.120 for WC1, where $\theta_c = 0.008\text{-}0.013$ and RS = 0.103 for WC2 and WC3, where $\theta_c = 0.020\text{-}0.033$ (Tables 1, A1 and A3, and Figure 2). This is the background current shear stress limiting the growth of wave ripples with increasing effect, such that for the strongest current the steepness is only just above the threshold for boundary-layer separation and vortex ejection (RS > 0.1, Sleath, 1984). Compared to the large ripples, the steepness of the small ripples was 0.04, implying there was no boundary layer separation (Figure 6a and Wu et al., 2022).

Other than this reduction in steepness, current strength was found to have a modest influence on ripple geometry; for example, RSI ≈ 1.5 for the large ripples for WC2 and WC3 (Table 2), compared to RSI ≈ 1.4 for WC1 (Wu et al., 2022). However, previous flume experiments with an increasing current

component have shown a more dramatic effect (Yokokawa, 1995, Dumas et al., 2005, Perillo et al., 2014). Perillo et al. (2014) found that ripples became more asymmetric, with RSI increasing from 1.4 to 1.7, as U_c increased from 0.1 to 0.3 m s^{-1}, with U_o = 0.25 m s^{-1}. The relatively coarse sediment used in WC1-WC3, D_{50} = 0.45 mm, may have resulted in a greater tendency towards 2D symmetric ripples, compared to Perillo et al.'s (2014) finer sediment, D_{50} = 0.25 mm, forming more 3D asymmetric ripples (Cummings et al., 2009, Pedocchi and García, 2009).

Figure 6b shows that the non-dimensional equilibrium wavelength, λ_e/D_{50}, is approximately constant for $C_0 \leq 7.4\%$. However, unlike the ripple steepness, there is a gradual linear reduction with C_0 for $C_0 >$ 7.4%. Interestingly, this 7.4% limit is very similar to the 8% limit at the base of the active layer discussed above. Based on the trend lines fitted to the data in Figure 6b, the clean-sand equivalent equilibrium ripple wavelengths fall into two distinct groups: a wave-dominant group, comprising the WC1 and Wu et al. (2018) cases where λ_e/D_{50} = 278, and a wave-current group, comprising the WC2 and WC3 cases where λ_e/D_{50} = 329 (18% larger). All ripples with $C_0 \leq 10.6\%$ are clearly 2D and orbital in nature (Figure 4a–d; Figure 3a–d in Wu et al., 2022 and Wu et al., 2018), including such characteristic features as bifurcations (Perron et al., 2018), implying that the wavelength is directly proportional to the wave orbital diameter. This together with the fact that skin friction stresses show that the flow can reverse ($\theta_w > \theta_c$), even for WC3 conditions, implies that the wavelength should be described by $\lambda_e = \alpha d_{wc}$, where α is the constant of proportionality (= 0.62, according to Wiberg and Harris, 1994) and d_{wc} is the orbital diameter enhanced by the current. Appendix B explains how d_{wc} is determined based on a sinusoidal wave. The value of d_{wc} is open to some interpretation, as the near-bed wave orbital diameter is combined with the depth-averaged current. Here, it has been chosen to reflect the difference in the clean-sand values of λ_e/D_{50} between the two groups: d_{wc}/D_{50} = 469 and 539, for the wave-dominant and wave-current groups, respectively. Wiberg and Harris' (1994) definition confirms that these flows are both within the orbital ripple regime ($d_{wc}/D_{50} \leq 1754$).

With the wave-current orbital diameter, d_{wc}, now determined it is possible to calculate the quantity α (= λ_e/d_{wc}), which is shown in Figure 6c. While there is scatter (R^2 = 0.762), all the data collapses onto a single curve with a similar behaviour to the wavelength (Figure 6b):

$$\alpha = \begin{cases} 0.61, & C_0 \leq C_{0m}, \\ 0.61 - 3.36(C_0 - C_{0m}), & C_0 > C_{0m}, \end{cases} \quad (6)$$

where $C_{0m} = 7.4\%$, such that $\alpha = 0.31$ when $C_0 = 16.3\%$. For $C_0 \leq 7.4\%$, ripples are orbital (α is

315 constant), and the constant is very close to Wiberg and Harris' (1994) clean-sand value, 0.62. For $C_0 >$

7.4%, where α reduces, the ripples effectively become increasingly anorbital in character.
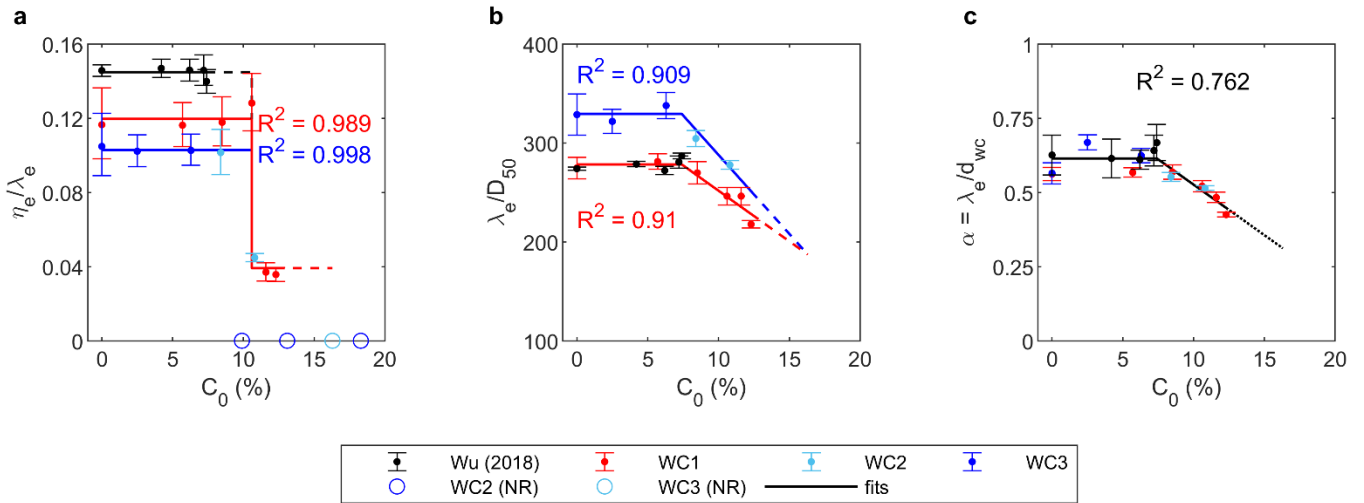
Figure 6. Equilibrium ripple steepness, $RS = \eta_e/\lambda_e$, (a), non-dimensional ripple wavelength, λ_e/D_{50},

(b) and the α parameter, $\alpha = \lambda_e/d_{wc}$, (c) as a function of initial bed clay content, C_0, for Wu et al.

320 (2018) and WC1-WC3. Open circles show that no ripples (NR) were present and dots are based

on measured values of η_e, λ_e and α and their error bars. Solid lines correspond to least-square-fits

to the data with R^2-values quoted.

4.2 The enhanced threshold of motion

The phase diagram of Figure 2 shows several cases without ripples (NR) (cf. Figure 6a and Table 2),

325 despite the skin friction being above the clean-sand threshold of motion ($C_0 \geq 16.3\%$ for WC2 and $C_0 \geq$

9.9% for WC3). The explanation for this discrepancy is that the clean-sand threshold of motion is

enhanced by the presence of the clay. According to Whitehouse et al. (2000), for $C_0 \leq 30\%$ the

enhanced threshold of motion can be expressed generically as

$$\theta_{0E} = \theta_0(1 + P_\theta C_0), \quad (7)$$

where P_θ is usually taken to be 20, but it can be anywhere in the range $7 \le P_\theta \le 45$. For WC1-WC3 and

330 Wu et al. (2018), where $D_{50} = 0.45$ and 0.496 mm, respectively, the clean-sand threshold is $\theta_0 = 0.032$. For combined colinear wave–current flow, $\theta_{0E} = \theta_w + \theta_c$. This results in the threshold line in Figure 2 moving diagonally upward towards the upper right-hand corner with increasing C_0. If θ_{0E} for WC1-WC3 and Wu et al. (2018) is to be consistent with the bed characterisations (Tables 1, A1 and A3), it is necessary for $\theta_{0E} < \theta_w + \theta_c$, when ripples are present (R), and $\theta_{0E} > \theta_w + \theta_c$, when ripples are absent (NR).

335 With $P_\theta = 20$, for WC3 and $C_0 \ge 9.9\%$, $\theta_{0E} \ge 0.095 > \theta_w + \theta_c$, which is consistent with the R/NR bed characterisations. However, for WC2 and $C_0 = 16.3\%$, $\theta_{0E} = 0.136 < \theta_w + \theta_c$, which is inconsistent with its NR characterisation (Table 1). Taking $C_0 = 16.3\%$ (WC2) as the limiting case, $\theta_{0E} = \theta_w + \theta_c = 0.155$, this gives a higher P_θ of 23 in Equation 7 which restores consistency and is still within Whitehouse et al.'s (2000) range. Figure 7a–f shows the magnitude of the time-varying skin friction using

$$\theta = |\theta_w \cos\sigma t + \theta_c|, \tag{8}$$

340 where $\sigma = 2\pi/T$ and the values of θ_w and θ_c are obtained from Tables 1, A1 and A3, compared with θ_{0E} using Equation 7 with $P_\theta = 23$ (yellow line). For all wave-only and wave-current cases, the above threshold (rippled-bed) and below threshold (flat-bed) cases are grouped together. Figure 7g shows the initiation time, t_i, when ripples begin to develop, from Tables 2, A1 and A3. In all cases, the skin friction is above threshold for only a fraction of the wave cycle. For each hydrodynamic condition, as

345 the threshold increases with increasing C_0, these wave-cycle fractions above threshold decrease, with a corresponding increase in t_i (Figure 7g), until the flat-bed cases, where the skin friction is always below threshold (Figure 7e and f). In each below threshold case there is an additional dashed line, which corresponds to the threshold based on the clay content at the end of the experiments (Figure 5f, g, h and k). WC2 and $C_0 = 16.3\%$, which is just above threshold at the end of the experiment (Figure 7f), and

350 WC3 and $C_0 = 6.4\%$, which is just below threshold, by about the same amount (Figure 7a), this new enhancement ($P_\theta = 23$ in Equation 7) is consistent with all combined wave-current and wave-only cases (Tables 1, A1 and A3).
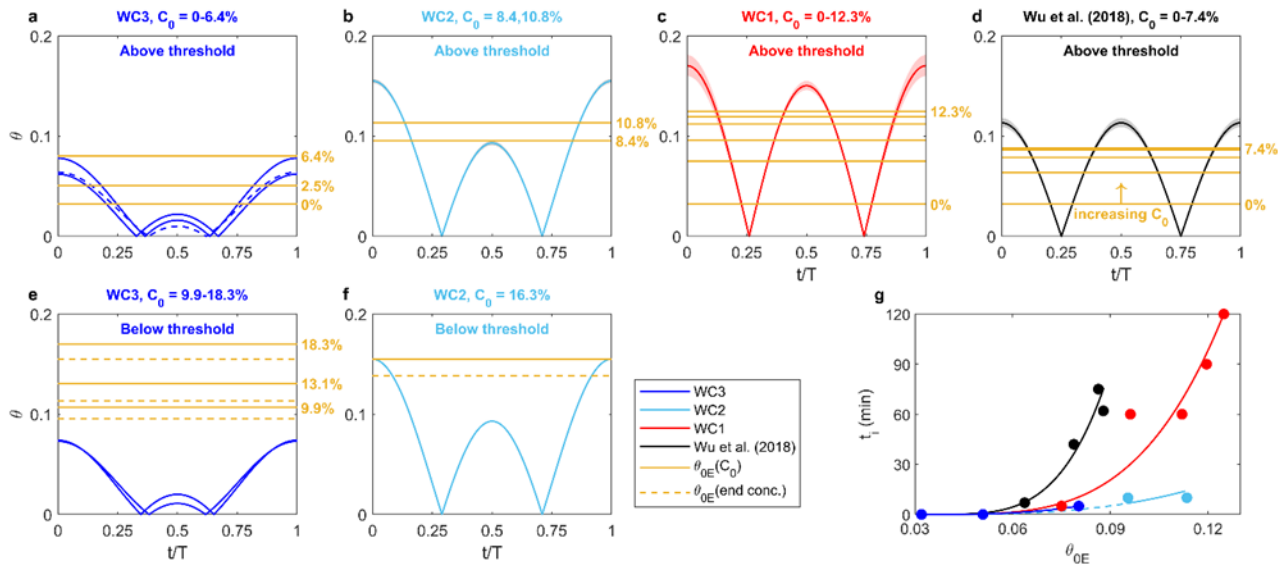
Figure 7. Time-varying skin friction using Equation 8 compared to θ_{0E} using Equation 7 with $P_\theta = $ 23, for the above- and below-threshold WC3 cases (a, e) and WC2 cases (b, f) and the above-threshold WC1 cases (c) and Wu et al. (2018) wave-only cases (d); and the initiation time, t_i, versus θ_{0E} (g), grouped according to flow condition. The legend applies to all panels. In (a) the dashed blue line corresponds to the $C_0 = 6.4\%$ case; in (c, d) the shaded region corresponds to the range of instantaneous skin friction values and in (e, f) the below threshold cases show an additional dashed line for θ_{0E} corresponding to the final sediment concentration.

In Baas et al.'s (2013) fine-sand, current-only experiments (Table A2), runs with $C_0 \geq 5.4\%$ were below the enhanced threshold, $\theta_c < \theta_{0E}$, based on Equation 7 with $P_\theta = 20$. This is inconsistent with the observations, as ripples appeared in these runs, indicating that this enhancement is too strong for $D_{50} = $ 0.143 mm. Baas et al. (2019) found a far more modest threshold enhancement of $P_\theta = 3$ in their threshold experiments for a similar grain size ($D_{50} = 0.142$ mm), where the velocity was stepped up sequentially over mixtures of sand and kaolinite clay until motion was detected. However, Baas et al.'s (2019) enhancement is a conservative estimate, since there was likely a cumulative effect of the sequential velocity steps, winnowing some of the clay from the bed before the threshold was passed for the sand grains. Figure 7 clearly shows that for the wave-only and wave-current cases, the initiation time is related to the fraction of the wave cycle when shear stresses are above threshold. However, the

current-only cases are fundamentally different as a substantial initiation time infers that the bed *must* initially be below threshold. In Baas et al.'s (2013) experiments, the C_0 = 16.2 and 18% cases resulted in substantial initiation times (Table A2). Since the experiment with C_0 = 13.8% of Baas et al. (2013) did not have a substantial initiation time, it can be assumed to be above threshold. Taking the lowest θ_c

375   for large ripples (C_0 = 11.8%) to represent the limiting case ($\theta_{0E} = \theta_c$); this gives P_θ = 6.4 in Equation 7, which is within Whitehouse et al.'s (2000) accepted range and is then consistent with all Baas et al.'s (2013) current-only experiments.

The critical shear stress enhancement for all mixed sand–kaolinite experiments can therefore be expressed as

$$\theta_{0E} = \theta_0 \times \begin{cases} 1 + 6.4C_0, & D_{50} = 0.143 \text{ mm}, \\ 1 + 23C_0, & 0.45 \leq D_{50} \leq 0.50 \text{ mm}, \end{cases} \quad (9)$$

380   where θ_0 = 0.061, for D_{50} = 0.143 mm, and θ_0 = 0.032, for $0.45 \leq D_{50} \leq 0.5$ mm. Equation 9 states that there is a stronger enhancement of the threshold of motion for coarse sand compared to fine sand. This grain-size difference has been explained by van Rijn (1999) in terms of the clay content required to envelop a sand particle. Specifically, to completely envelop sand grains with a clay layer of thickness, d, the volumetric concentration of clay required can be expressed as an increasing function of d/D_{50}.

385   Therefore, for a given clay concentration, the ratio of d around the two sand sizes is given by 0.45/0.143 $\approx$ 3. Interestingly, this ratio is similar to the ratio of constants in Equation 9 for the two grain sizes. Thus, the thicker clay layer around the coarser grains likely causes increased enhancement of the threshold of motion, which has also been found in field observations (Harris et al., 2016). It can be expected that the Baas et al. (2021) field data, where D_{50} = 0.227 mm and $0.6 \leq C_0 \leq 5.4\%$, should have

390   a coefficient somewhere between 8 and 23. The coefficient would probably be closer to 8, as there was no obvious change in the threshold during the field campaign. However, it is difficult to be more specific as the dominant clay mineral in the sediment was illite rather than kaolinite and there is also the presence of extracellular polymeric substances (EPS) to consider (Malarkey et al., 2015; Baas et al., 2019).

4.3 The potential factors controlling the deep cleaning of clay

395

Significant clay loss beneath equilibrium ripples was observed in the $C_0 = 6.4\%$ (WC3) case (Figure 5e), as occurred for $C_0 \leq 10.6\%$ in WC1 (Wu et al., 2022). Wu et al. (2022) highlighted the process of deep cleaning of clay from the substrate after ripples reached equilibrium, with clay loss occurring in a layer approximately three to four times the ripple height below the equilibrium ripple base. However, the deep-cleaning effect was considerably weaker in the $C_0 = 8.4\%$ (WC2) case, despite the increased hydrodynamic forcing compared to WC3 (Figure 5i). In Figure 8, clay loss is quantified by the average mass flux of clay out of the bed over each experiment, F_b, given by I/t_d, where t_d is the duration of the experiment, allowing the rippled- and flat-bed cases to be compared with one another. For large ripples, $F_b \approx 3.5 \times 10^{-6}$ g mm^{-2} min^{-1} under WC1 and WC3 conditions, whereas it decreased to 9.4×10^{-7} g mm^{-2} min^{-1} under WC2 conditions. By comparing ripple migration to pore water velocity magnitude, Wu et al. (2022) demonstrated winnowing dominance over hyporheic processes for WC1. While winnowing dominance is undoubtedly also the case for WC2 and WC3 in the active layer (Figure 5e and i), it is not necessarily the case below the active layer. In fact ripple migration rates were faster for WC2 conditions, $23 - 34$ mm min^{-1}, than for WC1 and WC3 conditions, $5 - 20$ and $8 - 13$ mm min^{-1}, respectively. For N$_2$O cycling beneath current ripples, Jiang et al. (2022) showed that increasing ripple migration can result in directional changes of hyporheic pore water flow in the bed from vertical to horizontal, potentially inhibiting clay removal or in the extreme case trapping the clay at depth. In the $C_0 = 8.4\%$ case, c. 20% of the clay was still able to be removed from a thin layer of approximately 20 mm beneath the active layer (Figure 5i); suggesting that pore water direction did not change completely from vertical to horizontal. F_b decreased to c. 8.5×10^{-7} g mm^{-2} min^{-1} for small ripples under WC1 and WC2 conditions, which is comparable to the large ripple flux for WC2. This suggests strong bed cohesion, as well as ripple migration, controls clay winnowing at depth (Teitelbaum et al., 2021; 2022). Further study is needed to quantify the relationship between ripple migration and clay winnowing efficiency.

420

A similar difference in deep cleaning between WC2 and WC3 was observed in the cases where no ripples formed (NR): $F_b = 4.8 \times 10^{-8}$ g mm^{-2} min^{-1} for WC3 and $F_b = 1.9 \times 10^{-8}$ g mm^{-2} min^{-1} for WC2. For flat beds, Higashino et al. (2009) found that increasing the shear velocity, u_*, increases the pore

water velocity, but decreases its penetration depth. If u_* is proportional to $\theta_{rms}^{½} = (½\theta_w^2+\theta_c^2)^{¼}$, where θ_{rms} is the root-mean-square of the instantaneous shear stress (Equation 8), then u_* is 50% larger for

425 WC2 than for WC3, suggesting that the ability of WC2 conditions to remove clay at depth is reduced. Compared to rippled beds, the fluxes from flat beds are two orders of magnitude smaller; this is consistent with previous studies showing that hyporheic exchange is enhanced by the presence of bedforms (Huettel et al., 1996; Packman et al., 2004; Higashino et al., 2009). Furthermore, Figure 8 shows the general stepping down of the flux as C_0 increases; this is probably an indication of the clay

430 forming blocked layers as can occur in sand-silt mixtures (e.g., Bartzke et al., 2013) which reduces permeability and also hydraulic conductivity, thus inhibiting the clay's removal.

Ignoring changes in porosity and cohesion, the hydraulic conductivity is approximately proportional to D_{10m}^2, where D_{10m} is the 10th percentile of the sand–clay mixture (Chapuis, 2012). For the mixture, there is little overlap in the sand and clay size distributions, $D_{50} >> D_{50c}$, where D_{50c} is the median diameter of

435 the clay particles (~ 0.009 mm) and $D_{10} = 0.34, 0.3$ and 0.072 mm for the sand in the Wu et al. (2018), WC1-3 and Baas et al. (2013) cases. As C_0 increases, D_{10m}, and therefore the conductivity, will decrease gradually. However, when $C_0 \geq 10\%$, D_{10m} switches from its approximate clean-sand value (~ D_{10}) to a much smaller size associated with the clay (~ D_{50c}), resulting in a 3-orders of magnitude reduction for the Wu et al. (2018) and WC1-3 cases and a 2-orders of magnitude reduction for Baas et al. (2013).

440 This ==reduction in hydraulic conductivity alone==, does not fully explain the behaviour seen in Figure 8, as there are the effects of changes in permeability and erosion threshold to consider as well. However, it may be the reason for the drastic change in ripple steepness at $C_0 = 10.6\%$, for the Wu et al. (2018) and WC1-3 cases (Figure 6a), and at the slightly higher value of $C_0 = 13\%$, for the Baas et al. (2013) cases, discussed in section 4.1.
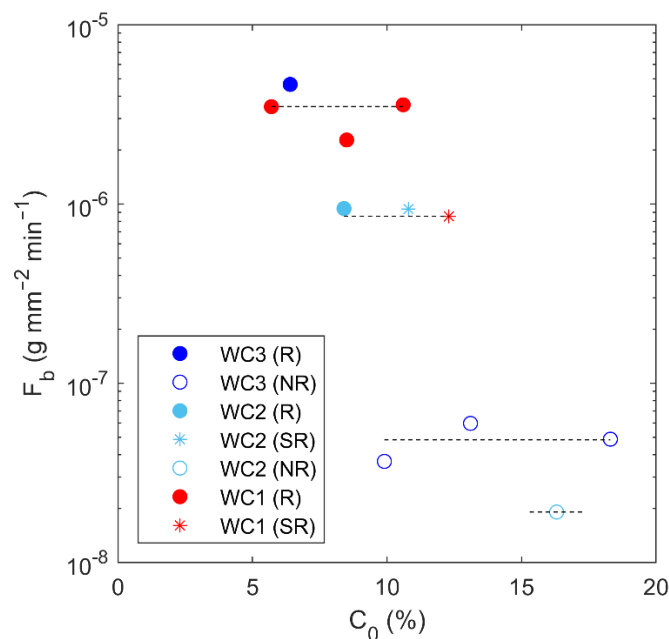
445

Figure 8. Average clay mass flux out of the bed, F_b, against initial clay content, C_0, for the WC2 and WC3 cases shown in Figure 6 together with WC1 for $C_0 = 5.7$, 8.5, 10.6 and 12.3% (Wu et al., 2022), where R, SR and NR signify large, small and no ripples.

4.4 Implications for paleowave climate predictions and bedform phase diagrams

450   The reduction in ripple wavelength with increasing C_0, and specifically how it relates to the orbital diameter through Equation 6, may have consequences for paleoenvironmental reconstruction. Based on orbital ripples preserved in the rock record, Diem (1985) used $\alpha = 0.65$ to determine the orbital diameter and hence the palaeowave climate, which included water depth and wave height and period. Thus, it is likely that if α is lowered by the presence of clay this would underpredict the ancient orbital diameter,

455   resulting in inaccurate paleowave climate predictions.

As proposed by Schindler et al. (2015), clay content can be incorporated into 3D phase diagrams. This has been done in Figure 9a and b by making use of Equation 9 and separating all the data depicted in Figure 2 into the two different grain-size ranges: $0.45 \leq D_{50} \leq 0.5$ mm and $D_{50} = 0.143$ mm (for the latter case only the current shear stress axis is shown as there is insufficient data for the full 3D plot). In

460   this new 3D phase diagram framework, there are four main regions: no motion (NM), ripples (R), small

ripples (SR), and washed-out ripples (WO). The upper boundary of NM is the yellow surface described by $\theta_w + \theta_c = \theta_{0E}$, where θ_{0E} is given by Equation 9, such that $\theta_{0E} = \theta_0$ when $C_0 = 0\%$. The NM region gradually expands with increasing C_0. This expanding region means the threshold eventually reaches the washout limit, $\theta_{0E} = \theta_{wo}$, where the ripple height starts to decrease near sheet flow conditions. Here,

465 $\theta_{0E} = \theta_{wo}$ corresponds to $C_0 = 19.6\%$, for $0.45 \leq D_{50} \leq 0.5$ mm, and $C_0 = 30.9\%$, for $D_{50} = 0.143$ mm, which is broadly consistent with Whitehouse et al.'s (2000) lower limit of between 20 and 30% for cohesive erosion in mixtures of sand and clay.

In Figure 9a, the large and small ripple regions are each subdivided into three subregions: wave-dominant (W and SW; $\theta_c < 0.2\theta_w$), wave-current (WC and SWC; $0.2\theta_w < \theta_c < 3.3\theta_w$), and current-

470 dominant (C and SC; $\theta_c > 3.3\theta_w$). The C/SC subdivision is shown in Figure 9b. Figure 9a also shows 2D cross-sections viewed from the $C_0 = 0\%$ end: (i) $0 \leq C_0 \leq 5.7\%$; (ii) $5.7 < C_0 \leq 10.6\%$; and (iii) $10.6 < C_0 \leq 19.6\%$, and marked in the 3D plot for reference. In Figure 9b for $D_{50} = 0.143$ mm, the small current ripples for $C_0 = 16.2\%$ and 18% appear in the NM region because it is thought that these cases were initially below threshold, as explained in Section 4.2. It is also likely that these ripples had not

475 reached equilibrium (Table A2; Baas et al., 2013). This illustrates the point that this phase diagram is dynamic: even if the flow conditions place the data in the no movement region for sand, or indeed the washout region, clay can still be winnowed out of the bed as it was in some of the WC3 and WC2 cases (Figure 5f, g, h and k).

The predictions of this new 3D phase diagram framework, show a dramatic reduction in bedform size

480 and therefore form roughness, which is proportional to η^2/λ. In the specific case of Baas et al.'s (2021) intertidal field site in the Dee Estuary, on which the 2D phase diagram (Figure 2) is based, there were no instances of smaller flatter ripples, which is consistent with the range of C_0 measured: $0.6 \leq C_0 \leq 5.4\%$. However, considering the widespread occurrence of mixed sand and mud flats (Murray et al., 2019), the scenario that an increase in the threshold shear stress in the presence of clay significantly

485 affects the state of the bed could occur frequently. Thus, it is likely that ripple dimensions could have been commonly overestimated by existing ripple predictors, potentially affecting the performance of morphodynamic models. The applicability of these 3D phase diagrams therefore requires further testing in muddy environments.
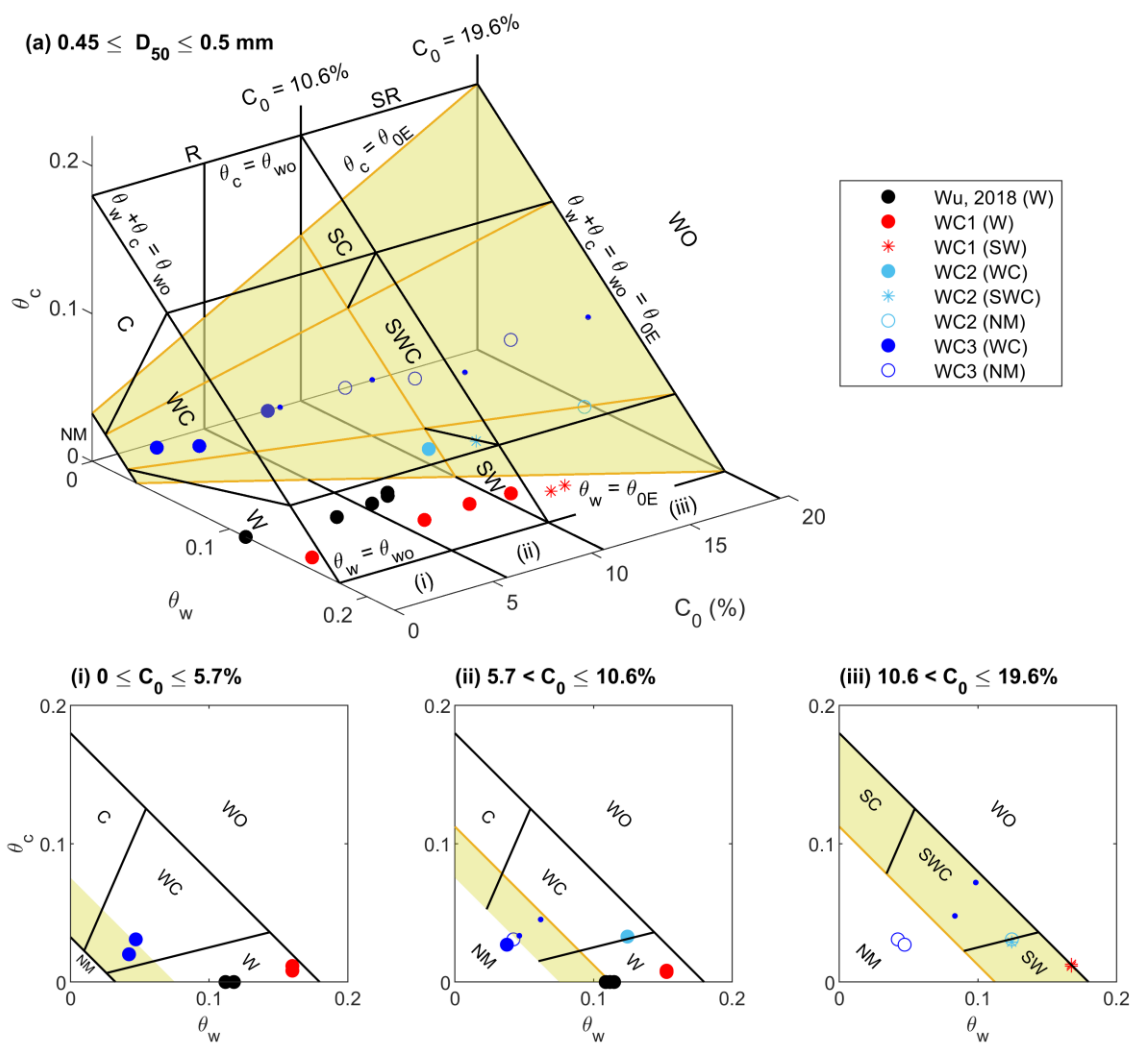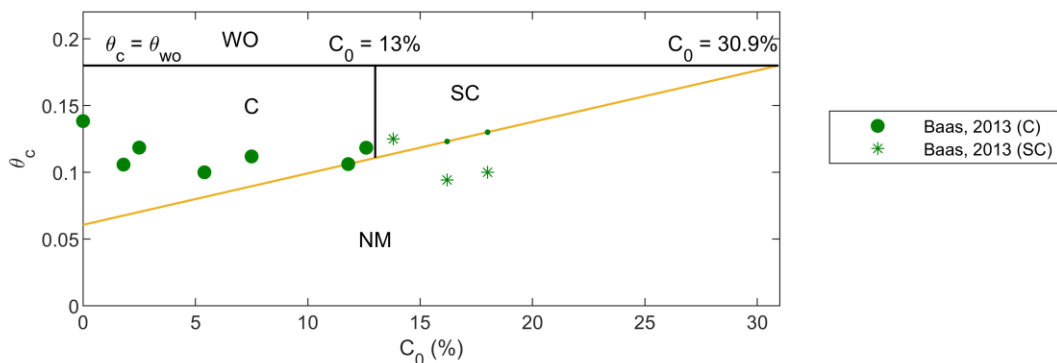
Figure 9.   Orthographic projection of the 3D phase diagram with clay dependence for $0.45 \leq D_{50} \leq$ 0.50 mm (a) and 2D C_0-θ_c plot for $D_{50} = 0.143$ mm (b), with the enhance critical shear stress, θ_{0E}, based on Equation 9, represented as the yellow surface. Below threshold cases have appropriately coloured small dots to mark the critical shear stress on the surface. In (a) there are also three 2D cross-sections viewed from the $C_0 = 0\%$ end: (i) $0 \leq C_0 \leq 5.7\%$ (ii) $5.7 < C_0 \leq 10.6\%$

495

and (iii) $10.6 < C_0 \leq 19.6\%$ and marked in the 3D plot. Solid circles: large ripples (R), asterisks: small ripples (SR), open circles: no ripples, C: current-dominant, WC: wave-current and W: wave-dominant (S prefix for small ripples), NM: no motion and WO: washout.

Conclusions

The present experiments examined ripple dynamics on cohesive beds under two different combined

500   wave–current conditions: WC2 ($U_o \approx 0.27$ m s^{-1}; $U_c \approx 0.31$ m s^{-1}) and WC3 ($U_o \approx 0.14$ m s^{-1}; $U_c \approx 0.31$ m s^{-1}). The experiments showed that under WC3 conditions ripples with similar dimensions and geometries to their clean-sand counterparts developed when initial clay content was $C_0 \leq 6.4\%$. These ripples were steep, 2D and quasi-symmetric in geometry (ripple steepness, RS = 0.11; ripple symmetry index, RSI = 1.5), with equilibrium heights and wavelengths, $\eta_e \approx 15$ mm, $\lambda_e \approx 148$ mm. Under WC2

505   conditions, for $C_0 = 8.4\%$, less steep, 2D and quasi-asymmetric (RS = 0.09 and RSI = 1.4) equilibrium ripples developed, with $\eta_e = 13.9$ mm, $\lambda_e = 137$ mm. However, for $C_0 = 10.8\%$, equilibrium ripple dimensions drastically decreased to $\eta_e = 5.6$ mm, $\lambda_e = 125$ mm, and the ripples transformed to flatter, 3D and asymmetric geometries (RS = 0.04 and RSI = 1.6).

Combining the present experiments with previous wave-only and wave-current experiments (Wu et al.,

510   2018; 2022) demonstrates the existence of a large to small equilibrium ripple discontinuity at $C_0 = 10.6\%$, with two distinct steepness groupings, RS ≥ 0.09 and RS ≈ 0.04, which is probably related to a three-orders of magnitude decrease in the hydraulic conductivity. The large ripple steepnesses show a decrease from 0.14 to 0.1 with increasing current strength. Ripple wavelength was independent of initial clay content when $C_0 \leq 7.4\%$, but it decreased linearly with initial clay content for $C_0 > 7.4\%$. For $C_0 \leq$

515   7.4%, the wavelength was proportional to the current-enhanced orbital diameter, d_{wc}, so that $\lambda_e = \alpha d_{wc}$,

where $\alpha = 0.61$. For $C_0 > 7.4\%$, α decreased linearly, which could be important for paleoenvironment reconstruction, when λ_e is measured and d_{wc} is unknown.

During the experiments, clay winnowing removed clay from both the active layer (crest to trough) and deep beneath it. Winnowing was quantified by the average mass flux of clay out of the bed, F_b. The flux was larger from large ripples, $F_b \approx 3.5 \times 10^{-6}$ g mm^{-2} min^{-1}, with the exception of the $C_0 = 8.4\%$ case under WC2 conditions ($F_b = 9.4 \times 10^{-7}$ g mm^{-2} min^{-1}). The flux decreased significantly by up to 2 two orders of magnitude to $F_b \approx 8.5 \times 10^{-7}$ and 1.9×10^{-8} g mm^{-2} min^{-1} for small ripples and flat beds, respectively.

The initiation time increased with initial clay content, and ultimately the bed remained flat when the initial clay content was large enough ($C_0 \geq 9.9\%$ and $C_0 \geq 16.3\%$ for WC3 and WC2 conditions, respectively), demonstrating the enhancement of the threshold of sediment motion with increased initial clay content. When combined with the fine-sand, current-only experimental results of Baas et al. (2013) this allowed the enhancement of the threshold to be quantified for both coarse ($0.45 \leq D_{50} \leq 0.5$ mm) and fine ($D_{50} = 0.143$ mm) mixed sand–clay motion. On the basis of these enhancements, new 3D phase diagrams, involving the non-dimensional wave and current shear stresses and C_0 are proposed to characterise the two ripple size groupings under different flow conditions. This new 3D phase diagram framework should prove important to the morphodynamic modelling community.

Appendices

Appendix A: Experimental conditions of Wu et al., (2022), Baas et al. (2013) and Wu et al. (2018).

Table A1. Wave-current experiments of Wu et al. (2022), where $h = 400$ mm, $T = 2$ s, $D_{50} = 0.45$ mm, $\nu = 1.12$ mm^{2}s^{-1} and $\rho = 1000$ kg m^{-3} and referred to in the main text as WC1 ($\theta_0 = 0.032$). Bedforms developed in all cases (R). *This fit is based on fitting two stages to the growth (see Wu et al., 2022)

C_0 (%)	U_0 (mm/s)	U_c (mm/s)	θ_w (-)	θ_c (-)	η_e (mm)	T_η (min)	λ_i (mm)	λ_e (mm)	T_λ (min)	t_i (min)
0	320	160	0.160	0.008	14.4±1.8	90	80.7±10.8	123.6±4.9	170	0
5.7	320	190	0.160	0.012	14.7±1.1	125	91.3±6.3	126.5±3.5	330	5

8.5	310	160	0.153	0.008	14.3±1.0	432	80.2±11.6	121.4±5.1	456	60
10.6*	310	150	0.153	0.007	13.7±1.0	678	92.6±10.2	110.9±4.0	540	60
11.6	330	190	0.168	0.012	4.1±0.4	271	84.5±10.0	108.5±2.6	382	90
12.3	330	200	0.168	0.013	3.5±0.3	211	71.7±6.3	98.0±1.7	499	120

Table A2. Current-alone experiments of Baas et al. (2013), with $U_0 = 0$ mm/s ($\theta_w = 0$), $D_{50} = 0.143$ mm, $\nu = 1.02$ mm^{2}s^{-1} and $\rho = 1000$ kg m^{-3} ($\theta_0 = 0.061$). Bedforms developed in all cases (R). *Equilibrium not reached after 2 h.

C_0	h	U_c	θ_c	η_e	T_η	λ_i	λ_e	T_λ	t_i
(%)	(mm/s)	(mm/s)	(-)	(mm)	(min)	(mm)	(mm)	(min)	(min)
0	248	400	0.138	16.2±0.5	64±8	28.5	116.3±3.5	81±16	0
1.8	250	350	0.106	13.6±0.8	53±10	46.1	95.5±3.9	83±20	3
2.5	247	370	0.118	14.1±0.8	40±8	40.2	115.3±5.6	69±19	5
5.4	248	340	0.100	13.3±0.8	74±12	35.7	98.4±8.2	87±34	5
7.5*	250	360	0.112	10.5±0.6	68±10	65.8	113.4±48.7	320±449	7
11.8	246	350	0.106	9.6±0.6	44±8	52.2	86.7±5.8	70±40	4
12.6	248	370	0.118	11.8±0.6	50±7	57.4	119.3±28.0	196±154	5
13.8	246	380	0.125	5.3±0.4			77.7±3.6		4
16.2	247	330	0.094	2.5±0.6			51.4±5.4		44
18.0	247	340	0.100	4.0±0.3			79.4±4.2		83

Table A3. Wave-alone experiments of Wu et al. (2018), with $U_c = 0$ mm/s ($\theta_c = 0$), $h = 600$ mm, $T = 2.48$ s, $D_{50} = 0.496$ mm, $\nu = 1.14$ mm^{2}s^{-1}, $\rho = 1015$ kg m^{-3} and $U_0 = \frac{1}{2}(U_{won}+U_{woff}) \pm\frac{1}{2}(U_{won}-U_{woff})$, where U_{won} and U_{woff} are the onshore and offshore freestream velocities ($\theta_0 = 0.032$). Bedforms developed in all cases (R).

C_0	U_0	θ_w	η_e	T_η	λ_i	λ_e	T_λ	t_i
(%)	(mm/s)	(-)	(mm)	(min)	(mm)	(mm)	(min)	(min)
0	275±25	0.112	19.8±0.3	27±5	87.5±8.5	135.9±0.8	40±4	0

4.2	285±25	0.118	20.3±0.5	27±14	101.2±12.4	138.5±1.3	66±7	7
6.2	280±20	0.115	19.7±0.5	76±17	97.4±12.2	135.0±2.0	105± 32	42±17
7.2	275±15	0.112	20.3±0.7	120±38	109.1±8.8	139.2±3.0	184± 43	75±35
7.4	270±20	0.109	19.9±0.7	122±55	103.1±8.4	142.3±1.5	200± 68	62±34

545

Appendix B: Determining the effective orbital diameter under combined flow

For a colinear sinusoidal wave and current, the horizontal velocity close to the bed is

$$u_{wc} = U_o(\cos\varphi + b), \qquad\qquad \text{B1}$$

where $\varphi = \sigma t$ is the phase of the wave, $\sigma = 2\pi/T$, t is time, $b = AU_c/U_o$ and A is constant ($A < 1$ as the near-bed current will be less than the depth-averaged current velocity). Figure B1 shows Equation B1

550 graphically. The orbital diameter, which is the horizontal distance moved between the two flow reversals for the positive wave half cycle is shown by the shaded area under the curve. The zero-crossing phase is given by

$$\varphi_0 = \arccos[\max(-b, -1)]. \qquad\qquad \text{B2}$$

When $b \geq 1$, $\varphi_0 = \pi$; there are no zero crossings, and only a single minimum. The effective orbital diameter, d_{wc}, corresponding to the shaded area in Figure B1 is

$$d_{wc} = 2\sigma \int_0^{\varphi_0} u_{wc}\,d\varphi = d_0(\sin\varphi_0 + b\varphi_0), \qquad\qquad \text{B3}$$

555 where $d_0 = U_o T/\pi$ (Soulsby, 1997) is the orbital diameter for the wave alone, when $b = 0$. For the wave-current experiments, the value of A used in the parameter b was $A = 0.1, 0.22$ and 0.42 for WC1, WC2 and WC3, respectively, and for the wave-alone Wu et al. (2018) experiments $d_{wc} = d_0$ since $b = 0$.
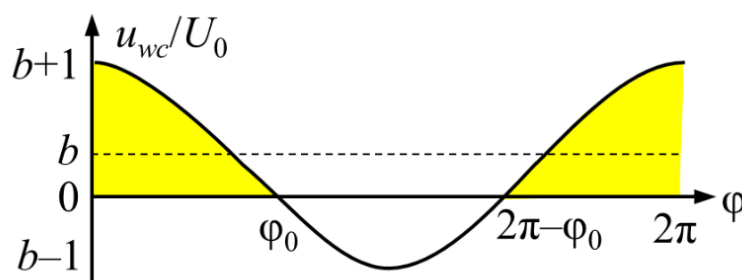
Figure B1. Plot of Equation B1, where shaded area represents d_{wc} in Equation B3.

Data availability

Supporting data are available through figshare which is a free and open repository (Wu et al., 2023).

Author contribution

XW and RF designed and carried out experiments. XW, JM, RF and EP processed experimental data. XW prepared the original manuscript. JM, JB, RF, and DP reviewed and edited the manuscript. DP acquired project funding and supervised the project.

Competing interests

DP is member of the editorial board of journal *Earth Surface Dynamics*. The peer-review process was guided by an independent editor, and the authors have also no other competing interests to declare.

Acknowledgments

The authors acknowledge the enormous contributions of Brendan Murphy, whose help throughout the study made our setup, data collection, and clean-up efforts smooth and trouble free. The authors acknowledge Oliver Dawes and the Hull Marine Laboratory at the University of Hull for their support in processing grain sizes with the Malvern Mastersizer 2000. Participation of XW, JM, RF, JHB, EP and DRP was made possible thanks to funding by the European Research Council under the European Union's Horizon 2020 research and innovation program (grant no. 725955). Participation of RF was also supported by the Leverhulme Trust and Leverhulme Early Career Researcher Fellowship (grant ECF-2020-679).

References

Arnott, R. W. & Southard, J. B. 1990. Exploratory flow-duct experiments on combined-flow bed configurations, and some implications for interpreting storm-event stratification. *Journal of Sedimentary Research,* 60, 211-219.

Baas, J. H., Baker, M. L., Malarkey, J. Bass, S. J., Manning, A. J., Hope, J. A., Peakall, J., Lichtman, I. D., Ye, L., Davies, A. G., Parsons, D. R., Paterson, D. M. & Thorne, P. D. 2019. Integrating field and laboratory approaches for ripple development in mixed sand–clay–EPS. *Sedimentology,* 66, 2749-2768.

Baas, J., Malarkey, J., Lichtman, I. D., Amoudry, L. O., Thorne, P., Hope, J. A., Peakall, J., Paterson, D. M., Bass, S. & Cooke, R. D. 2021. Current-and Wave-Generated Bedforms on Mixed Sand–Clay Intertidal Flats: A New Bedform Phase Diagram and Implications for Bed Roughness and Preservation Potential. *Frontiers Earth Science,* 9, 747567.

Baas, J. H., Davies, A. G. & Malarkey, J. 2013. Bedform development in mixed sand–mud: The contrasting role of cohesive forces in flow and bed. *Geomorphology,* 182, 19-32.

Bartzke, G., Bryan, K. R., Pilditch, C. A. & Huhn, K. 2013. On the stabilizing influence of silt on sand beds. *Journal of Sedimentary Research,* 83, 691-703.

Beard, J. A., Bush, A. M., Fernandes, A. M., Getty, P. R. & Hren, M. T. 2017. Stratigraphy and paleoenvironmental analysis of the Frasnian-Famennian (Upper Devonian) boundary interval in Tioga, north-central Pennsylvania. *Palaeogeography, Palaeoclimatology, Palaeoecology,* 478, 67-79.

Brakenhoff, L., Schrijvershof, R., van der Werf, J., Grasmeijer, B., Ruessink, G. & van der Vegt, M. 2020. From ripples to large-scale sand transport: The effects of bedform-related roughness on hydrodynamics and sediment transport patterns in delft3d. *Journal of Marine Science and Engineering,* 8, 892.

Chapuis, R.P., 2012. Predicting the saturated hydraulic conductivity of soils: a review. *Bulletin of Engineering Geology and the Environment*, 71, 401-434.

Cummings, D. I., Dumas, S. & Dalrymple, R. W. 2009. Fine-grained versus coarse-grained wave ripples generated experimentally under large-scale oscillatory flow. *Journal of Sedimentary Research,* 79, 83-93.

Diem, B. 1985. Analytical method for estimating palaeowave climate and water depth from wave ripple marks. *Sedimentology,* 32, 705-720.

Dumas, S., Arnott, R. & Southard, J. B. 2005. Experiments on oscillatory-flow and combined-flow bed forms: implications for interpreting parts of the shallow-marine sedimentary record. *Journal of Sedimentary research,* 75, 501-513.

Gao, S. 2019. Geomorphology and sedimentology of tidal flats. *Coastal Wetlands.* Elsevier.

Harris, R. J., Pilditch, C. A., Greenfield, B. L., Moon, V. & Kröncke, I. 2016. The influence of benthic macrofauna on the erodibility of intertidal sediments with varying mud content in three New Zealand estuaries. *Estuaries and Coasts,* 39, 815-828.

Healy, T., Wang, Y. & Healy, J.-A. 2002. *Muddy coasts of the world: processes, deposits and function*, Elsevier.

Héquette, A., Hemdane, Y. & Anthony, E. J. 2008. Sediment transport under wave and current combined flows on a tide-dominated shoreface, northern coast of France. *Marine geology,* 249, 226-242.

Higashino, M., Clark, J.J. & Stefan, H.G., 2009. Pore water flow due to near‐bed turbulence and associated solute transfer in a stream or lake sediment bed. *Water resources research,* 45(12), W12414, doi: 10.1029/2008WR007374.

Huettel, M., Ziebis, W. & Forster, S., 1996. Flow‐induced uptake of particulate matter in permeable sediments. *Limnology and Oceanography,* 41(2), 309-322.

Jiang, Q., Liu, D., Jin, G., Tang, H., Wei, Q. & Xu, J., 2022. N2O dynamics in the hyporheic zone due to ripple migration. *Journal of Hydrology,* 610, 127891.

Khelifa, A. & Ouellet, Y. 2000. Prediction of sand ripple geometry under waves and currents. *Journal of waterway, port, coastal, and ocean engineering,* 126, 14-22.

630   Kleinhans, M. 2005. Phase diagrams of bed states in steady, unsteady, oscillatory and mixed flows. In *SANDPIT, Sand Transport and Morphology of Offshore Sand Mining Pits*, L.C. van Rijn, R.L. Soulsby, P. Hoekstra and A.G. Davies (editors), Aqua Publications, Amsterdam, Paper Q.

Li, M. Z. & Amos, C. L. 1999. Field observations of bedforms and sediment transport thresholds of fine sand under combined waves and currents. *Marine Geology,* 158, 147-160.

635   Malarkey, J., Baas, J. H., Hope, J. A., Aspden, R. J., Parsons, D. R., Peakall, J., Paterson, D. M., Schindler, R. J., Ye, L. & Lichtman, I. D. 2015. The pervasive role of biological cohesion in bedform development. *Nature communications,* 6, 6257, doi: 10.1038/ncomms7257.

Malarkey, J. & Davies, A. G. 2012. A simple procedure for calculating the mean and maximum bed stress under wave and current conditions for rough turbulent flow based on method. *Computers & Geosciences,* 43, 101-107.

640

Mousavi, M. E., Irish, J. L., Frey, A. E., Olivera, F. & Edge, B. L. 2011. Global warming and hurricanes: the potential impact of hurricane intensification and sea level rise on coastal flooding. *Climatic Change,* 104, 575-597.

Murray, N.J., Phinn, S.R., DeWitt, M., Ferrari, R., Johnston, R., Lyons, M.B., Clinton, N., Thau, D. and Fuller, R.A., 2019. The global distribution and trajectory of tidal flats. *Nature*, 565, 222-225.

645

Myrow, P., Snell, K., Hughes, N., Paulsen, T., Heim, N. & Parcha, S. 2006. Cambrian depositional history of the Zanskar Valley region of the Indian Himalaya: tectonic implications. *Journal of Sedimentary Research,* 76, 364-381.

Osborne, P. D. & Greenwood, B. 1993. Sediment suspension under waves and currents: time scales and vertical structure. *Sedimentology,* 40, 599-622.

650

Packman, A.I., Salehin, M. & Zaramella, M., 2004. Hyporheic exchange with gravel beds: Basic hydrodynamic interactions and bedform-induced advective flows. *Journal of Hydraulic Engineering*, 130(7), 647-656.

Pedocchi, F. & García, M. 2009. Ripple morphology under oscillatory flow: 2. Experiments. *Journal of Geophysical Research: Oceans,* 114, C12015, doi:10.1029/2009JC005356.

655

Perillo, M. M., Best, J. L. & Garcia, M. H. 2014. A new phase diagram for combined-flow bedforms. *Journal of Sedimentary Research,* 84, 301-313.

Perron, J. T., Myrow, P. M., Huppert, K. L., Koss, A. R. & Wickert, A. D. 2018. Ancient record of changing flows from wave ripple defects. *Geology,* 46, 875-878.

Precht, E. & Huettel, M. 2003. Advective pore‐water exchange driven by surface gravity waves and its ecological implications. *Limnology and Oceanography,* 48, 1674-1684.

Rogers, C., Dijkstra, T. & Smalley, I. 1994. Particle packing from an Earth science viewpoint. *Earth-Science Reviews,* 36, 59-82.

Sleath, J. F. A., 1984. *Seabed Mechanics*. Wiley.

Sumer, B. M., Whitehouse, R. J. & Tørum, A. 2001. Scour around coastal structures: a summary of recent research. *Coastal Engineering,* 44, 153-190.

Tanaka, H. & Dang, V. T. 1996. Geometry of sand ripples due to combined wave-current flows. *Journal of waterway, port, coastal, and ocean engineering,* 122, 298-300.

Teitelbaum, Y., Dallmann, J., Phillips, C.B., Packman, A.I., Schumer, R., Sund, N.L., Hansen, S.K. and Arnon, S., 2021. Dynamics of hyporheic exchange flux and fine particle deposition under moving bedforms. *Water Resources Research*, 57(4), p.e2020WR028541.

Teitelbaum, Y., Shimony, T., Saavedra Cifuentes, E., Dallmann, J., Phillips, C.B., Packman, A.I., Hansen, S.K. and Arnon, S., 2022. A novel framework for simulating particle deposition with moving bedforms. *Geophysical Research Letters*, 49(4), p.e2021GL097223.

van den Berg, J. & van Gelder, A. 1993. A new bedform stability diagram, with emphasis on the transition of ripples to plane bed in flows over fine sand and silt. *Special Publications of the International Association of Sedimentologists,* 17, 11-21.

van Rijn, L.C., 1999. Erodibility of Mud-Sand Bed Mixtures. *Journal of Hydraulic Engineering,* 146(1), 04019050.

Vercruysse, K., Grabowski, R. C. & Rickson, R. 2017. Suspended sediment transport dynamics in rivers: Multi-scale drivers of temporal variation. *Earth-Science Reviews,* 166, 38-52.

Vitousek, S., Barnard, P. L., Fletcher, C. H., Frazer, N., Erikson, L. & Storlazzi, C. D. 2017. Doubling of coastal flooding frequency within decades due to sea-level rise. *Scientific reports,* 7, 1-9.

Whitehouse, R., Soulsby, R., Roberts, W. & Mitchener, H. 2000. *Dynamics of Estuarine Muds: A Manual for Practical Applications*, Thomas Telford.

Wiberg, P. L. & Harris, C. K. 1994. Ripple geometry in wave‑dominated environments. *Journal of Geophysical Research: Oceans,* 99, 775-789.

Wu, X., Baas, J. H., Parsons, D. R., Eggenhuisen, J., Amoudry, L., Cartigny, M., Mclelland, S., Mouazé, D. & Ruessink, G. 2018. Wave Ripple Development on Mixed Clay‑Sand Substrates: Effects of Clay Winnowing and Armoring. *Journal of Geophysical Research: Earth Surface,* 123, 2784-2801.

Wu, X., Fernández, R., Baas, J.H., Malarkey, J. & Parsons, D.R. 2022. Discontinuity in equilibrium wave-current ripple size and shape and deep cleaning associated with cohesive sand-clay beds. *Journal of Geophysical Research Earth Surface*, 127, e2022JF006771.

Wu, X., Malarkey, J., Fernandez, R., Baas, J. H., Parsons, D.R. (2023): Flume experiments to investigate the influence of cohesive clay on wave-current ripple dynamcis. figshare. Dataset. https://doi.org/10.6084/m9.figshare.22578529.v1

Yokokawa, M. 1995. Combined-flow ripples: genetic experiments and applications for geologic records. *Series D, Earth and planetary sciences*. 29 (1), 1-38, 1995-12-26, Faculty of Science, Kyushu University.